

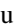





# Energy Conversion between Ions and Electrons through Ion Cyclotron Waves and Embedded Ion-scale Rotational Discontinuity in Collisionless Space Plasmas

Qiaowen Luo<sup>1,2</sup>, Jiansen He<sup>2</sup> , Jun Cui<sup>1</sup> , Xingyu Zhu<sup>2</sup> , Die Duan<sup>2</sup>, and Daniel Verscharen<sup>3,4</sup> 

<sup>1</sup>School of Atmospheric Sciences, Sun Yat-sen University, Zhuhai 519000, People's Republic of China

<sup>2</sup>School of Earth and Space Sciences, Peking University, Beijing 100871, Beijing, People's Republic of China; [jshept@pku.edu.cn](mailto:jshept@pku.edu.cn)

<sup>3</sup>Mullard Space Science Laboratory, University College London, Dorking RH5 6NT, UK

<sup>4</sup>Space Science Center, University of New Hampshire, Durham, NH, USA

Received 2020 August 15; revised 2020 October 23; accepted 2020 November 2; published 2020 November 25

## Abstract

Wave–particle interaction is a fundamental process in collisionless plasma, which results in the redistribution of energy between plasma waves and particle species. The analysis of high-resolution Magnetospheric Multiscale plasma and magnetic field data directly reveals the energy exchange between electromagnetic energy, particle bulk kinetic energy, and thermal kinetic energy in magnetosheath turbulence. This work focuses on the energy transfer associated with ion cyclotron waves (ICWs) and embedded rotational discontinuity (RD). We find that (1) the particle kinetic energy of ions is converted into electromagnetic energy; (2) the electrons are gaining energy from electromagnetic fields, having significant electron heating in the parallel direction around the RD; (3) the ICWs and RD connect and redistribute energy between ions and electrons in the postshock downstream sheath region; and (4) the interactions between pressure tensor and strain tensor redistribute the ion and electron bulk and thermal kinetic energies, but less significantly than direct field–particle interaction by one order of magnitude in the ICW turbulence with weak compressibility, in the sense that  $(d|\mathbf{B}|/|\mathbf{B}|)^2 < 10^{-2}$ ,  $(dN/N)^2 < 10^{-2}$ .

*Unified Astronomy Thesaurus concepts:* Interplanetary turbulence (830); Space plasmas (1544); Solar wind (1534)

## 1. Introduction

Wave–particle interactions play a crucial role in energy conversion between turbulent energy and kinetic energy in collisionless space plasmas, in which the motion of charged particles is controlled by electromagnetic fields (Tu & Marsch 1995; He et al. 2019; Kitamura et al. 2018; Telloni et al. 2019; Chen et al. 2019; Parashar & Gary 2019). According to its polarization properties, the wave-like turbulence at kinetic scales can be characterized as ion-cyclotron-like, kinetic-(inertial-)Alfvén-like, or whistler-like in its dynamics (Leamon et al. 1998; Gary & Smith 2009; He et al. 2011; Chen & Boldyrev 2017). It is oblique kinetic-Alfvén-like turbulence, rather than whistler-like turbulence that dominates the dissipation of solar wind turbulence near the proton kinetic scales (He et al. 2012). Ion cyclotron waves (ICWs) are usually observed in different solar–terrestrial environments, i.e., in Earth’s magnetosphere, magnetosheath, and solar wind (Dunlop et al. 2002; Wicks et al. 2016; Zhao et al. 2018). The plasma thermal states (thermal anisotropy and plasma  $\beta_{\parallel}$ ) associated with ICWs are often found to be around the instability threshold indicating the possible generation mechanism due to ion cyclotron instability (Woodham et al. 2019; Zhao et al. 2019). Large-amplitude electromagnetic ICWs will have an influence on the dynamics of charged particles, which result in a periodic variation of the ion pitch angle. Besides, the electron pitch angle exhibits a localized feature on a timescale comparable to the wave period (Zhao et al. 2019). ICWs are found to be dissipated in magnetosheath turbulence, driving the proton temperature distribution into an anisotropic kinetic state (He et al. 2019). The dissipation rate spectrum was calculated for the first time by He et al. (2019). Kitamura et al. (2018) have recently provided direct quantitative evidence for collisionless energy transfer in magnetospheric plasmas between distinct particle populations via

wave–particle interactions. He et al. (2015) revealed the coexistence of two wave modes (quasi-parallel ICWs and quasi-perpendicular kinetic Alfvén waves (KAWs)) and three resonance diffusion plateaus in proton velocity space, which suggests a complicated scenario of wave–particle interactions in solar wind turbulence: left-handed cyclotron resonance between ICWs and the proton core population, and Landau and right-handed cyclotron resonances between KAWs and the proton beam population. The field–particle correlation method has been successfully implemented to study the energy transfer in Landau damping of (kinetic) compressive waves in simulations (Klein & Howes 2016; Ruan et al. 2016; Howes 2018) as well as in observations (Chen et al. 2019).

The turbulence is often intermittent, and it is still unclear what the nature of the intermittent fluctuations is. The intermittent structures are categorized as various types of discontinuities as well as the boundaries of pressure-balanced structures (Wang et al. 2013). A pair of back-to-back rotational discontinuities (RDs) is often found to bound the reconnection exhaust region, which is also bounded by a pair of slow-shock-like discontinuities (Whang et al. 1998). RDs at the boundaries of reconnection exhaust regions redirect the inflow plasma and confine them to the exhaust regions forming a dumbbell shape of the proton velocity distribution, which is strongly thermal anisotropic with  $T_{\parallel} > T_{\perp}$  and subject to the firehose instability (He et al. 2018). Zhang et al. (2019) showed in their simulation that ions are accelerated by the RD magnetic field tension and gain bulk flow energy, while electrons are controlled by the electric potential that results in a higher electron temperature. Therefore, both kinetic wave modes and intermittent structures are crucial in the energy transfer between fields and particles.

The  $\mathbf{J} \cdot \mathbf{E}$  term is often studied in observational time series and in simulation data to quantify the energy transfer between fields and particles at various scales (Yang et al. 2017; Chasapis et al. 2018; He et al. 2019). For the interaction

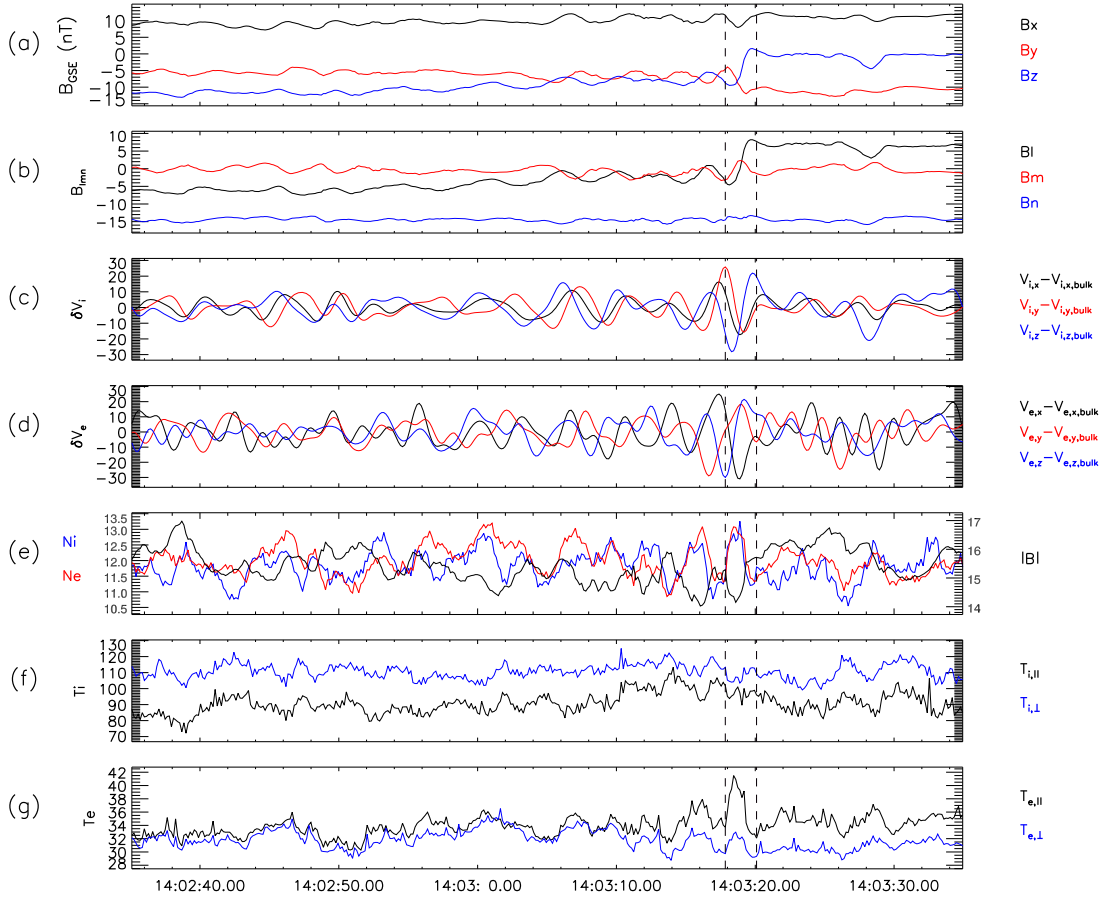


**Figure 1.** Overview of plasma and magnetic field measurements between 14:02:35 and 14:03:35 on 2017 October 7. (a) Time sequences of the magnetic field components in the GSE coordinates ( $B_x$ ,  $B_y$ ,  $B_z$ ). (b) Time series of the magnetic field components in global LMN coordinates ( $B_L$ ,  $B_M$ ,  $B_N$ ). (c) The fluctuating ion bulk velocity vectors ( $V_{ix}$ ,  $V_{iy}$ ,  $V_{iz}$ ) in 0.1–0.5 Hz with the mean bulk flow velocity averaged over the whole ICW interval (14:02:35–14:03:35) being subtracted. (d) The fluctuating electron bulk velocity vectors ( $V_{ex}$ ,  $V_{ey}$ ,  $V_{ez}$ ) in 0.1–0.5 Hz with the mean bulk flow velocity averaged over the whole ICW interval (14:02:35–14:03:35) being subtracted. (e) Ion and electron number densities and magnetic field strength  $|B|$ . The parallel and perpendicular temperatures of ions and electrons are illustrated in panels (f) and (g). The two black vertical dashed lines bound the interval of a rotational discontinuity (RD).

between ions and waves, the energy transfer rate is calculated as the dot product of the fluctuating electric field ( $E_{wave}$ ) and the fluctuating ion current ( $J_i$ ), both of which are perpendicular to the background magnetic field  $B_0$  in cyclotron-resonant interactions (Omura et al. 2010). Aside from the  $J \cdot E$  term, the term for the pressure–strain tensor interaction,  $-(P \cdot \nabla) \cdot V$ , is another proxy for energy dissipation, representing the energy conversion from bulk kinetic energy to thermal energy (Yang et al. 2017; Chasapis et al. 2018). Simulations suggest that, although scale-dependent, the spatial patterns of  $J \cdot E$  and  $-(P \cdot \nabla) \cdot V$  are often concentrated in proximity to each other (Yang et al. 2019).

The magnetosheath, compressed solar wind downstream of the bow shock, provides a unique laboratory for observational studies of plasma turbulence, in which kinetic-scale turbulence can be measured at high quality. The energy cascade rate in MHD turbulence in the compressible magnetosheath plasma was found to be at least two orders of magnitude higher than in the (nearly) incompressible solar wind (Hadid et al. 2018). How the energy is converted and dissipated at kinetic scales is another important issue. Using the Magnetospheric Multiscale (MMS; Burch et al. 2016) measurements, this study provides observational evidence for the energy conversion between waves and particles of space plasma turbulence in the magnetosheath when ICWs and RD are present. In the

following sections, we first study a typical ICW event that contains an RD. We then analyze  $J \cdot E$  and  $-(P \cdot \nabla) \cdot V$  for ions and electrons in this event, including the associated time series, the integration results, and the sign of the energy transfer and its magnitude. Finally, we present a physical scenario of ICWs and RD in the energy-conversion process.

## 2. Observations and Analyses

Since we investigate both particle and field behavior, we analyze MMS data from instruments including the Fast Plasma Investigation (FPI; Pollock et al. 2016) and FIELDS (Torbert et al. 2016) instruments. We choose an ICW event in magnetosheath during the time interval from 14:02:35 UT to 14:03:35 UT on 2017 October 7 (Zhao et al. 2018) for a comprehensive study. The LMN coordinates are obtained from global minimum variance analysis (MVA) of the magnetic field time sequences (Sonnerup & Scheible 1998). Figure 1 shows an overview of this event based on the plasma and magnetic field measurements. The jump of the vector magnetic field component  $B_z$  in the GSE coordinates (Figure 1(a)) and  $B_L$  in the global LMN coordinates (Figure 1(b)) is marked by two vertical black dashed lines.

The coherent ICWs concentrate in the frequency range  $0.1\text{ Hz} \leq f \leq 0.5\text{ Hz}$ . Therefore, this frequency range is selected as the filtered frequency. In Figures 1(c) and 1(d),

the disturbance of bandpassed ion bulk velocity (i.e., ion fluid velocity) and bandpassed electron bulk velocity around the characteristic frequency display a high correlation with the magnetic field disturbance during the whole ICW interval (14:02:35–14:03:35), and also shows a significant RD-related jump embedded in the ICW interval during 14:03:17–14:03:20. The time series of ion density, electron density, and magnetic field strength (Figure 1(e)) show compressive disturbances in addition to the ICWs and RD ( $(d|\mathbf{B}|/|\mathbf{B}|)^2 < 10^{-2}$ ,  $(dN/N)^2 < 10^{-2}$ ). There is a rising jump in  $N_i$  and  $N_e$  associated with a slightly declining jump in  $|\mathbf{B}|$  between the two black vertical dashed lines in Figure 1(e). The temperature of the ions (Figure 1(f)) shows a thermal anisotropy, where  $T_{i,\perp} > T_{i,\parallel}$ . It should be noted that, near RD, ions tend to be thermally isotropic (Figures 1(f)). In the time series of the electron temperature (Figure 1(g)), the electrons are approximately isotropic before the crossing of the RD, while at the RD,  $T_{e,\parallel}$  is significantly higher than  $T_{e,\perp}$ . The parallel temperature of the electrons shows an increase in Figure 1(g), suggesting that the electrons are heated in the parallel direction. The thermal anisotropy ( $T_{e,\parallel} > T_{e,\perp}$ ) continues in the time series after crossing the RD.

A Walén analysis of the positively correlated dB and dV jumps confirms the existence of an RD (see Figures 2(a) and (b)). The correlation coefficient between  $V \times B$  and  $V_{HT} \times B$  for the Walén test of the RD is 0.99. The correlation coefficient between local  $V_A$  and  $V - V_{HT}$  of the RD is 0.96. The change of the component  $B_N$  is small, indicating that the RD was propagating in the N-direction. The propagation speed of the HT frame after subtracting the bulk is about  $-80 \text{ km s}^{-1}$  in the N-direction, consistent with the Alfvén speed calculated from  $B_N$  ( $-84 \text{ km s}^{-1}$ ) in the N-direction.

Two snapshots of the velocity distribution function (VDF) of ions and electrons are illustrated in Figures 2(c) and (d), respectively. From the left to the right, the direction of the magnetic field experiences a significant change, consistent with the existence of our RD. Along with the rapid change of the magnetic field direction, we also observe the associated changes of i-VDFs and e-VDFs, which move synchronously in velocity space in phase with the magnetic field vector.

The oscillation of  $J \cdot E$  is shown in Figure 3. The contributions to the total current density from the ion and electron species are calculated separately as  $J_i = N_i \cdot q_i \cdot V_i$  and  $J_e = N_e \cdot q_e \cdot V_e$ . The electric field depends on the reference frame. We define  $E'_{\text{mean}} = E + \langle V \rangle \times B$  and  $E'_{\text{local}} = E + V \times B$  as the electric fields in the mean and local bulk flow reference frames. The mean bulk velocity  $\langle V \rangle$  is the bulk velocity (i.e., fluid velocity) averaged over the time interval (14:02:35–14:03:35) and is calculated separately for ions and electrons. He et al. (2019) demonstrated that it is more accurate to calculate the direct energy-conversion rate from the electromagnetic energy to the particle energy in the mean flow reference frame. Here, the current densities  $J_i$  and  $J_e$ , as well as the electric field  $E'$  are filtered in the frequency range  $0.1 \text{ Hz} \leq f \leq 0.5 \text{ Hz}$ . The work done by the electromagnetic field on ions in the local and mean bulk flow reference frames are illustrated in Figures 3(a) and 3(b). Likewise, we show the work done by the electromagnetic field on electrons in the local and mean bulk flow reference frames in Figures 3(e) and 3(f). We can see that the quantity of  $J \cdot E'$  oscillates between positive and negative for both ions and electrons. However, at the region of the RD, the work done by the electromagnetic

field on ions is negative, meaning that the bulk kinetic energy of ions is converted to the electromagnetic energy. On the contrary, positive work done by electromagnetic field on electrons can be observed, which indicates that the electromagnetic energy is converted into the bulk kinetic energy of electrons.

The integrated work done by the electromagnetic field on particles is shown in Figures 3(c) and (d) for ions and Figures 3(g) and (h) for electrons. For the chain of energy conversion between particles and fields associated with ICWs and RD in this exemplar case, we suggest that (1) the ion species plays the role of a source of energy; (2) the electron species acts as a sink of energy and experiences parallel heating with enhanced  $T_{e,\parallel}$ ; and (3) the ICWs and RD fields act as an intermediate bridge, converting energy from the ions to the electrons.

The work done by the action of the pressure tensor and strain-rate tensor,  $-(P \cdot \nabla) \cdot V$  in 0.1–0.5 Hz, is shown in Figure 4. The strain-rate tensor in  $-(P \cdot \nabla) \cdot V$  can be decomposed into the dilatation term and the traceless strain-rate tensor (Yang et al. 2017). The work done by the term “double contraction of deviatoric pressure tensor and traceless strain-rate tensor” (hereafter “Pi-D”) is also shown in Figure 4. Before crossing the RD,  $-(P \cdot \nabla) \cdot V$  (Figure 4(a)) and Pi-D (Figure 4(b)) for ions mostly oscillate around a positive value, leading to a secular net energy transfer from ion bulk kinetic energy to ion thermal energy. In the vicinity of the RD, both  $-(P_i \cdot \nabla) \cdot V_i$  and Pi-D are negative at first and later positive for the ions. At the first encounter with the RD,  $-(P_e \cdot \nabla) \cdot V_e$  for electrons is evidently positive (Figure 4(d)), leading to an increase of  $-\int (P_e \cdot \nabla) \cdot V_e dt$  at the corresponding time (Figure 4(f)). The positive  $-(P_e \cdot \nabla) \cdot V_e$  for electrons indicates that the bulk kinetic energy of electrons is converted into thermal energy, which possibly explains the observed parallel heating of electrons shown in Figure 1(g). According to Figure 4(e), Pi-D is positive during the whole RD encounter (14:03:17–14:03:20), which indicates that the Pi-D term potentially plays an important role for the heating of the plasma electrons in this time interval (14:03:17–14:03:20). However, if we take the whole ICW interval (14:02:35–14:03:35) into consideration, we can find that the dilatation term is the main contributor to converting the thermal kinetic energy into the bulk kinetic energy of electrons.

### 3. Summary and Discussion

We summarize our interpretation of the energy-conversion scenario in Figure 5. In this scenario, we can see that the bulk kinetic energies of ions are converted to the fluctuating electromagnetic fields of the ICWs as well as the embedded RD, with  $\int J_i \cdot E'_{\text{mean}} dt \sim -4 \times 10^{10} \text{ eV/m}^3$  for the interval of about 1 minute. On the other hand, the fluctuating electromagnetic energy of the ICWs and RD is converted to the bulk kinetic energies of electrons with  $\int J_e \cdot E'_{\text{mean}} dt \sim +4 \times 10^{10} \text{ eV/m}^3$ , which is opposite in sign but comparable in magnitude to  $\int J_i \cdot E'_{\text{mean}} dt$ . The ion bulk kinetic energy is converted to their thermal energy when taking the whole interval into consideration with  $-\int (P_i \cdot \nabla) \cdot V_i dt \sim 1 \times 10^9 \text{ eV/m}^3$ , which is smaller than  $\int J_i \cdot E'_{\text{mean}} dt$  by more than one order of magnitude. For the electrons, the energy is converted from thermal kinetic energy to bulk kinetic energy during the whole interval except the RD interval, which has positive  $-(P_e \cdot \nabla) \cdot V_e$  indicating the local heating with thermal kinetic energy converted from bulk kinetic energy.

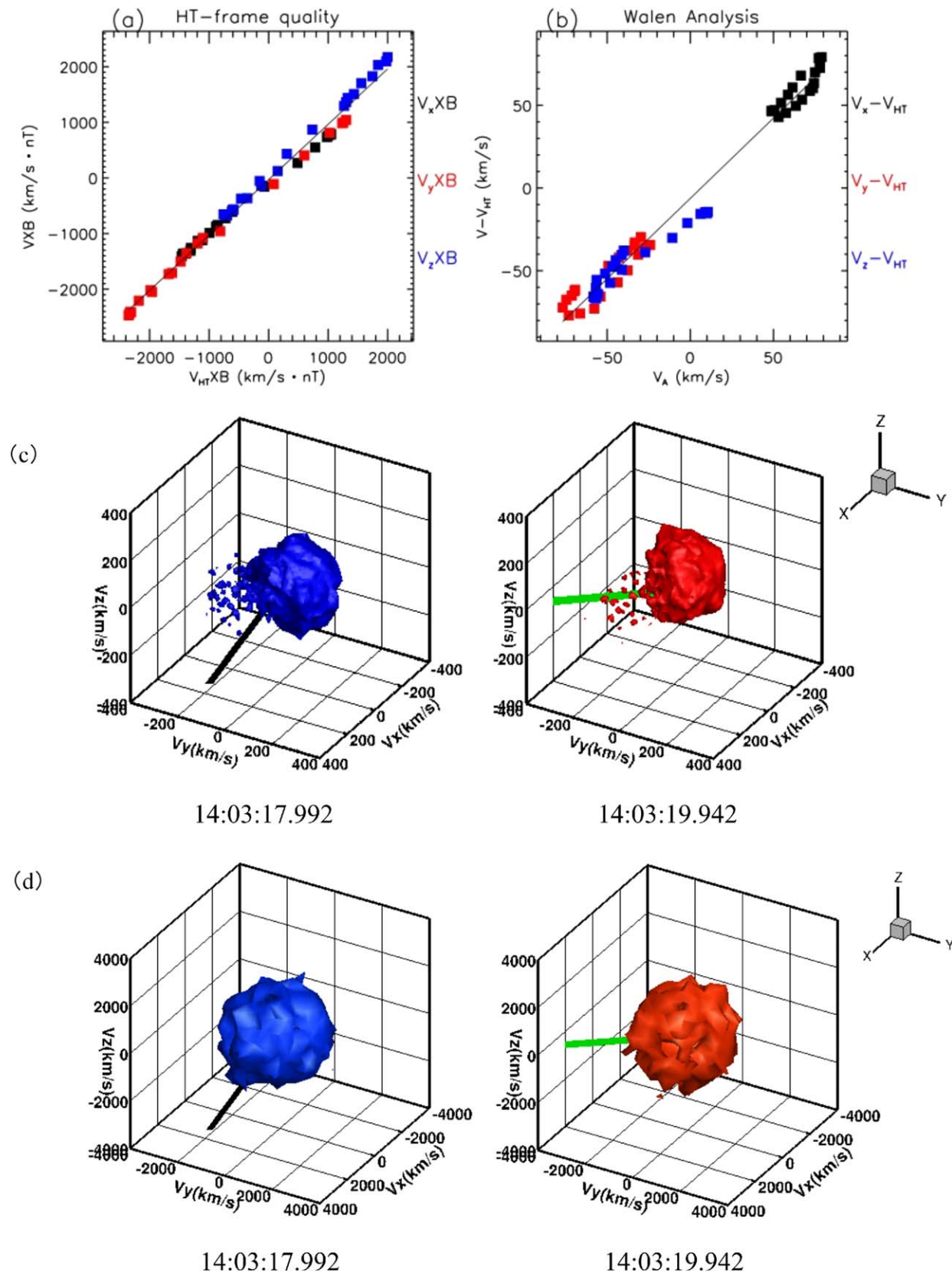


**Figure 2.** Walén analysis of the interval containing a possible RD and the 3D velocity distribution functions of protons and electrons (14:03:17–14:03:20). (a) The HT frame shows a good alignment in  $V_{HT} \times B$  with  $V \times B$ . (b) Comparison between  $V_A$  and  $V - V_{HT}$  shows a good correlation for the RD (black, red, and blue squares represent the scatterplots of the GSE x, y, and z components). (c) The velocity distribution functions of ions (p-VDF). (d) The velocity distribution functions of electrons (e-VDF). The contour levels of the p-VDF and e-VDF are selected as  $e^{-2}$  ( $\sim 0.13$ ) of their maximum VDF values. The straight lines represent the magnetic field directions.

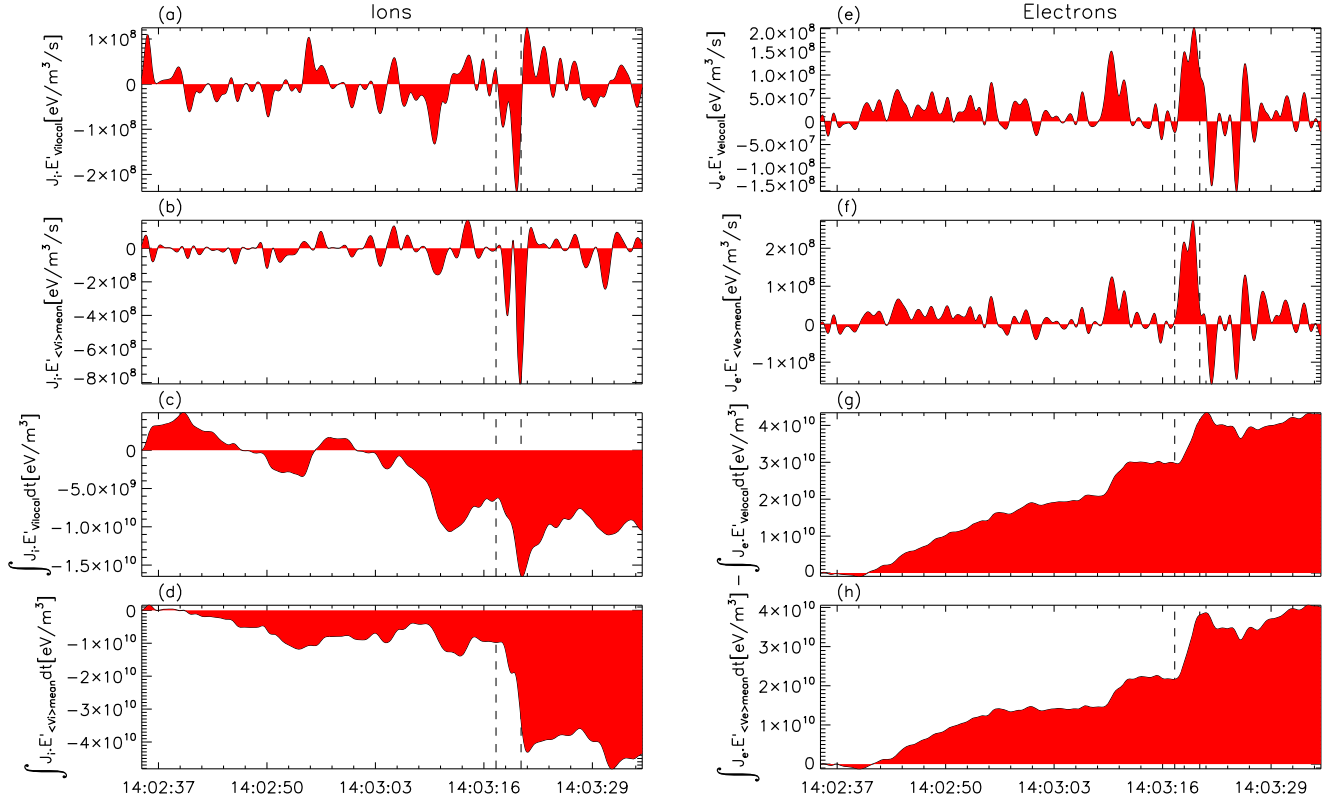


**Figure 3.** Work done by the electromagnetic field ions and electrons in 0.1–0.5 Hz. (a) and (b) The work done by the electromagnetic field on the ion species in the ion local and mean bulk flow reference frames, respectively. (c) and (d) The overall (i.e., time-integrated) work done by the electromagnetic field on the ion species in the ion local and mean bulk flow reference frames are illustrated, respectively. (e)–(h) The work and overall work done by the electromagnetic fields on the electrons in the electron local and mean bulk flow reference frames, respectively. The two black vertical dashed lines bound the interval of a rotational discontinuity (RD).

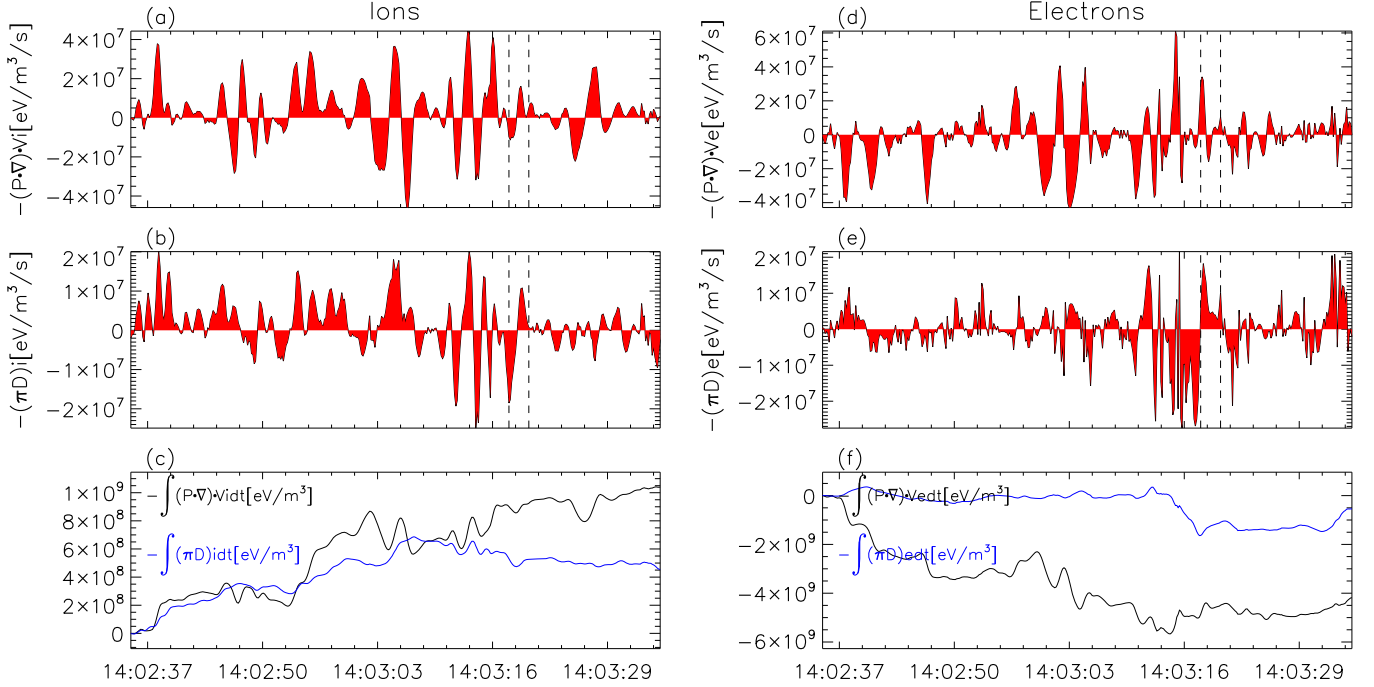


**Figure 4.** The work done by  $-(P \cdot \nabla) \cdot V$  in 0.1–0.5 Hz on ions and electrons, where the contribution of the traceless strain-rate tensor  $\text{Pi-D} (= -\pi\text{D})$  in 0.1–0.5 Hz is shown. The work done by  $-(P \cdot \nabla) \cdot V$  on ions and electrons is plotted in panels (a) and (d), while the contribution of the  $\text{Pi-D}$  term on ions and electrons is plotted in panels (b) and (e). The overall work done by  $-(P \cdot \nabla) \cdot V$  (the black lines) and  $\text{Pi-D}$  (the blue lines) on ions and electrons is illustrated in panels (c) and (f). The two black vertical dashed lines bound the interval of a rotational discontinuity (RD).

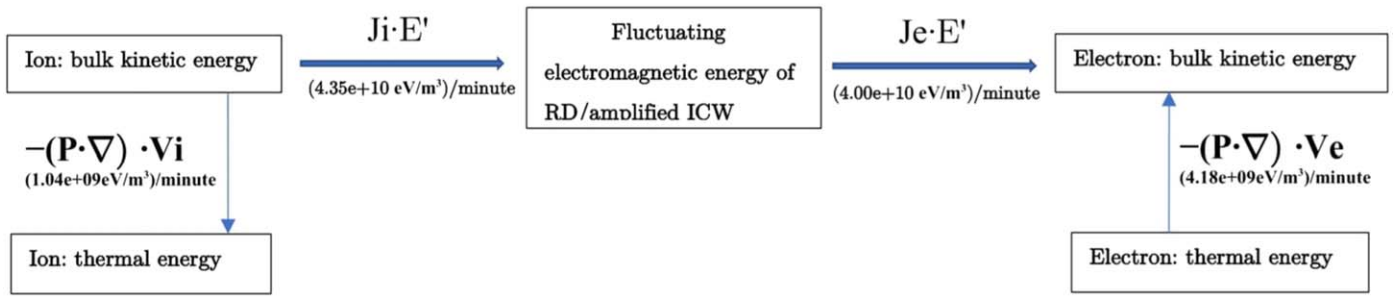


**Figure 5.** Flow chart of energy conversion related with kinetic-scale ICWs and the RD during the whole time interval (2017 October 7, 14:02:35–14:03:35) in 0.1–05 Hz. The bulk kinetic energy referred to the fluctuating bulk kinetic energy, the velocity of which has the mean bulk flow velocity subtracted.

From these results we conclude that, through the fluctuating electromagnetic fields of the observed ICWs and the embedded RD, the energy transfer from ions to electrons is achieved via the work done by electric fields on current carriers without collisions in collisionless space plasmas. Moreover, the approximate balance between the integrals for  $J_i \cdot E'$  and  $J_e \cdot E'$  seems to indicate a saturation of the growth or dissipation of the ICWs, which have comparable fluctuation magnitudes of ion and electron bulk velocities and are consistent with the eigenmode fluctuations as predicted by linear plasma theory. Furthermore, in weakly compressive structures such as those shown here, the action of the pressure tensor and strain-rate tensor, which are less than the work associated with the direct field–particle interaction and dominated by the traceless strain-rate term, should be taken into account for the energy conversion between bulk and thermal energy of the same particle species.

Our work investigates the energy conversion in magnetosheath plasma, which has undergone a preferential ion energization during the plasma’s bow-shock transition. Therefore, our scenario of energy conversion through ICWs and embedded RD is likely to be relevant to other astrophysical shock transitions. Based on the above perspective and the fact that shock and sheath exist widely in astrophysical plasmas, the result of this work is of scientific significance, because it provides an observational basis and physical scenario for the energy redeposition between different species of particles after a shock transition.

The authors are grateful to the teams of the MMS spacecraft for providing the data. The work at Peking University is supported by NSFC under contracts 41674171, 41874200, and 41421003. The work at Sun Yat-sen University is supported by NSFC through grants 41525015, 41774186, and 41525016. D.V. from UCL is supported by the STFC Ernest Rutherford Fellowship ST/P003826/1 and STFC Consolidated Grant ST/S000240/1. This work is also supported by CNSA under contract Nos. D020301 and D020302 and supported by the Key Research Program of the Institute of Geology & Geophysics, CAS, Grant IGGCAS 201904.

## ORCID iDs

Jiansen He <https://orcid.org/0000-0001-8179-417X>  
 Jun Cui <https://orcid.org/0000-0002-4721-8184>  
 Xingyu Zhu <https://orcid.org/0000-0002-1541-6397>  
 Daniel Verscharen <https://orcid.org/0000-0002-0497-1096>

## References

- Burch, J. L., Moore, T. E., Torbert, R. B., & Giles, B. L. 2016, *SSRv*, 199, 5  
 Chasapis, A., Yang, Y., Matthaeus, W. H., et al. 2018, *ApJ*, 862, 32  
 Chen, C., & Boldyrev, S. 2017, *APS*, CO6.002, 1  
 Chen, C. H. K., Klein, K. G., & Howes, G. G. 2019, *NatCo*, 10, 740  
 Dunlop, M. W., Lucek, E. A., Kistler, L. M., et al. 2002, *JGRA*, 107, 1228  
 Gary, S. P., & Smith, C. W. 2009, *JGRA*, 114, A12105  
 Hadid, L., Sahraoui, F., Galtier, S., & Huang, S. 2018, *AGUFM*, SM32A–02, 1  
 He, J., Marsch, E., Tu, C., Yao, S., & Tian, H. 2011, *ApJ*, 731, 85  
 He, J., Tu, C., Marsch, E., & Yao, S. 2012, *ApJL*, 745, L8  
 He, J., Wang, L., Tu, C., Marsch, E., & Zong, Q. 2015, *ApJL*, 800, L31  
 He, J., Zhu, X., Chen, Y., et al. 2018, *ApJ*, 856, 148  
 He, J., Duan, D., Wang, T., et al. 2019, *ApJ*, 880, 121  
 Howes, G. G. 2018, *PhPI*, 25, 055501  
 Kitamura, N., Kitahara, M., Shoji, M., et al. 2018, *Sci*, 361, 1000  
 Klein, K. G., & Howes, G. G. 2016, *ApJL*, 826, L30  
 Leamon, R. J., Matthaeus, W. H., Smith, C. W., & Wong, H. K. 1998, *ApJL*, 507, L181  
 Omura, Y., Pickett, J., Grison, B., et al. 2010, *JGRA*, 115, A07234  
 Parashar, T. N., & Gary, S. P. 2019, *ApJ*, 882, 29  
 Pollock, C., Moore, T., Jacques, A., et al. 2016, *SSRv*, 199, 331  
 Ruan, W., He, J., Zhang, L., et al. 2016, *ApJ*, 825, 58  
 Sonnerup, B. U. Ö., & Scheible, M. 1998, *ISSIR*, 1, 185  
 Telloni, D., Carbone, F., Bruno, R., et al. 2019, *ApJL*, 885, L5  
 Torbert, R. B., Russell, C. T., Magnes, W., et al. 2016, *SSRv*, 199, 105  
 Tu, C. Y., & Marsch, E. 1995, *SSRv*, 73, 1  
 Wang, X., Tu, C., He, J., Marsch, E., & Wang, L. 2013, *ApJL*, 772, L14  
 Whang, Y. C., Zhou, J., Lepping, R. P., et al. 1998, *JGR*, 103, 6513  
 Wicks, R. T., Alexander, R. L., Stevens, M., et al. 2016, *ApJ*, 819, 6  
 Woodham, L. D., Wicks, R. T., Verscharen, D., et al. 2019, *ApJL*, 884, L53  
 Yang, Y., Wan, M., Matthaeus, W. H., et al. 2019, *MNRAS*, 482, 4933  
 Yang, Y., Matthaeus, W. H., Parashar, T. N., et al. 2017, *PhRvE*, 95, 061201  
 Zhang, Q., Drake, J. F., & Swisdak, M. 2019, *PhPI*, 26, 072115  
 Zhao, G. Q., Feng, H. Q., Wu, D. J., Pi, G., & Huang, J. 2019, *ApJ*, 871, 175  
 Zhao, J. S., Wang, T. Y., Dunlop, M. W., et al. 2018, *ApJ*, 867, 58  
 Zhao, J. S., Wang, T. Y., Dunlop, M. W., et al. 2019, *GeoRL*, 46, 4545